Estimating sub-canopy shortwave irradiance to melting snow on forested slopes

Chad R. Ellis and John W. Pomeroy*

Centre for Hydrology, University of Saskatchewan, 117 Science Place, Saskatoon, Sask. S7N 5C8, Canada

Abstract:

Estimates of shortwave irradiance energy beneath needle-leaf forests over complex terrain are needed to drive energy balance snowmelt models and to evaluate the potential hydrological impacts of forest-cover change in mountain regions. This paper outlines and evaluates a physically-based model designed to estimate sub-canopy shortwave irradiance to snowcover under needle-leaf forest-cover with respect to surface slope and azimuth. Transmission of above-canopy irradiance was estimated using forest-surveys and hemispherical photographs to determine the fractions of forest-cover occupied by non-transmitting trunks, partially-transmitting crowns and fully-transmitting gaps with respect to above-canopy diffuse and direct beam shortwave irradiance. Simulations were conducted for continuous, uniform lodgepole pine forests on level site and a north facing slope and a discontinuous, non-uniform forest on a southeast facing slope during snowmelt at the Marmot Creek Research Basin, Alberta, Canada. Mean observed daily transmissivity values of irradiance were 0·09 at the north-facing forest, 0·21 at the level forest and 0·36 at the southeast-facing forest. Modelled and observed results indicate that potential snowmelt energy from sub-canopy shortwave irradiance is likely to exhibit the greatest variation with change in cloudiness and forest-cover density under south-facing forests and the least variation under north-facing forests. Comparisons of simulations to observations indicate that the model can explain much of the difference in daily shortwave transmission amongst sites, performing relatively poorest at the north-facing forest where fluxes were small and relatively best at the south-east facing forest where fluxes were large. However, simulation errors in terms of absolute irradiance were greatest at the southeast-facing forest, having a root mean square error (RMSE) 0·64 MJ m^{-2}d^{-1} compared to 0·44 MJ m^{-2}d^{-1} at the level forest and 0·27 MJ m^{-2}d^{-1} at the north-facing forest. Copyright © 2007 John Wiley & Sons, Ltd.

KEY WORDS   snow hydrology; sub-canopy radiation; forest transmissivity; snowmelt energy; needle-leaf forest; mountain hydrology; shortwave radiation

Received 1 June 2006; Accepted 30 January 2007

INTRODUCTION

Runoff from mountain snowmelt is the main contributor to the flow of many North American rivers in the western half of the continent (Marks and Winstral, 2001). The combination of high relief and forest-cover complicates the estimation of the shortwave irradiance to snowcover; shortwave and longwave radiation comprise the largest energy source driving sub-canopy melt (United States Army Corps of Engineers, 1956; Federer, 1968; Link and Marks, 1999; Sicart *et al.*, 2004). Thus, effective prediction of the timing and magnitude of mountain snowmelt runoff for the purposes of reservoir operation, land-use planning, and flood forecasting requires accurate estimation of shortwave irradiance transmission through sloping forest-covers.

The most basic methods of estimating forest transmission of shortwave irradiance employ the Poisson model, most prominently expressed as Beer-Bouger's Law in which the rate of shortwave irradiance extinction is determined by an extinction coefficient. However, application of such models to forests requires the assumption that forest foliage represents a continuous and homogenous

medium, composed of infinitely small attenuating elements of random orientation. In mountain environments such ideal conditions may not always be satisfied as the combination of topography and pronounced structuring of needle-leaf forests permits considerable transmission of shortwave irradiance through canopy gaps (Rowlands *et al.*, 2002; Melloh *et al.*, 2003). Also disregarded is the non-uniform distribution of the attenuating material of needle-leaf forests, composed of an assortment of solid trunks, open crowns and gaps that produce distinct patterns of irradiance and shadow upon sub-canopy snowcover (Figure 1). For these reasons, it is likely that effective estimations of shortwave irradiance under sloped needle-leaf forests will require more realistic representation of forest-cover heterogeneity than that afforded by simplified Beer-Bouger expressions.

More sophisticated methods estimate the sub-canopy shortwave irradiance by explicitly accounting for transmission through forest gaps and absorption by trunks and crowns. Here, individual trunk and crowns are often abstracted by simple geometric shapes (e.g. Federer, 1971; Satterlund, 1983; Rowland and Moore, 1992; Ni *et al.*, 1999; Stadt and Lieffers, 2000; Corbaud *et al.*, 2003) allowing their application to sloped surfaces. However, many such models require extensive calibration, which may not be possible due to the (i) vast

---

* Correspondence to: John W. Pomeroy, Centre for Hydrology, University of Saskatchewan, 117 Science Place, Saskatoon, Sask. S7N 5C8, Canada. E-mail: pomeroy@usask.ca

Figure 1. Scene beneath a mature lodgepole pine forest showing the distinct spatial patterns of irradiance and trunk shadows on the sub-canopy surface

combinations of surface orientations and forest-cover densities and (ii) the lack of sub-canopy irradiance measurements on sloped surfaces (Wang *et al.*, 2006). In addition, few such models have been evaluated for needle-leaf forests in which substantial differences in surface orientation exist.

OBJECTIVE

The objective of this paper is two-fold. The first is to outline a simple model designed to estimate sub-canopy shortwave irradiance through determination of (i) above-canopy irradiance corrected for topography and (ii) forest transmission of above-canopy shortwave irradiance with respect to surface orientation and forest-cover density. The second is to evaluate the model by comparing simulated and observed transmission of daily shortwave irradiance and the resulting sub-canopy irradiance energy for sites of varying forest-cover density and surface orientation.

MODEL OUTLINE

Forest-cover transmissivity (τ) to above-canopy shortwave irradiance may be defined as the ratio of sub-canopy (K_S) to above-canopy (K_O) shortwave irradiance:

$$\tau = \frac{K_S}{K_O} \tag{1}$$

In the model, τ is estimated by calculating the respective transmissivities of both above-canopy beam (K_B) and diffuse (K_D) irradiance. Here, K_B is considered to be received by forest-cover from the position of the solar disk, and K_D in equal intensity from across the remaining sky hemisphere unobstructed by topography. Net sub-canopy shortwave irradiance is thus the sum of beam and diffuse sub-canopy irradiance, including enhancement from multiple reflection between the snow surface

and forest-layer. The main procedures and simulation products of the model are outlined in Figure 2.

Estimation of above-canopy irradiance with respect to surface orientation

Hourly estimates of K_B and K_D were made by relating the diffuse fraction of total above-canopy shortwave irradiance (k_d) to an atmospheric transmissivity (clearness) index (k_T) via

$$k_d = 1 \cdot 1 - 1 \cdot 09\, k_T \tag{2}$$

in which k_T is calculated by

$$k_T = \frac{K_O}{K_{EX}} \tag{3};$$

where K_{EX} and K_O are the respective hourly exo-atmospheric and surface shortwave irradiance to a level surface. The coefficients in Equation (2) were resolved using trial and error with selection of those providing the best geometric correction of hourly observed level irradiance to a nearby surface of 27° slope gradient and 128° azimuth. Best correction of level irradiance (x_{mod}) was determined as that providing the smallest root mean square error (RMSE) Equation (4) to observed (x_{obs}) daily slope irradiance.

$$\text{RMSE} = \frac{1}{n}\sqrt{\sum_{i=1}^{n}(x_{mod} - x_{obs})^2} \tag{4}$$

Where n is the number of paired values examined. Figure 3 shows daily level shortwave and corrected level irradiance compared to observations of slope irradiance, including the RMSE of both.

Although the $k_d - k_T$ relation expressed in Equation (2) was determined by indirect means, it compares well to other relations developed by direct measurements of diffuse and total shortwave irradiance in North America. Figure 4 shows Equation (2) and $k_d - k_T$ relations developed from concurrent diffuse and total shortwave irradiance point measurements in Canada (e.g. Stadt *et al.*, 2005; Tuller, 1976) and the United States (e.g. Lui and Jordan, 1960).

Forest-transmissivity fractions

Forest transmissivities of K_D and K_B are estimated by determining the fractions of forest-cover occupied by (i) non-transmitting trunks (T_f) (ii) partially-transmitting crowns (C_f) and (iii) fully-transmitting gaps (G_f). Forest-fractions are calculated in order of least to greatest transmissivity, such that the area occupied by formerly resolved fraction(s) is unavailable to the next:

$$T_f = 0 \rightarrow 1 \tag{5}$$

$$C_f = 1 - T_f \tag{6}$$

$$G_f = 1 - (C_f + T_f) \tag{7}$$

Trunks and crowns are abstracted in the model by simple geometric shapes: right- circular cylinder trunks
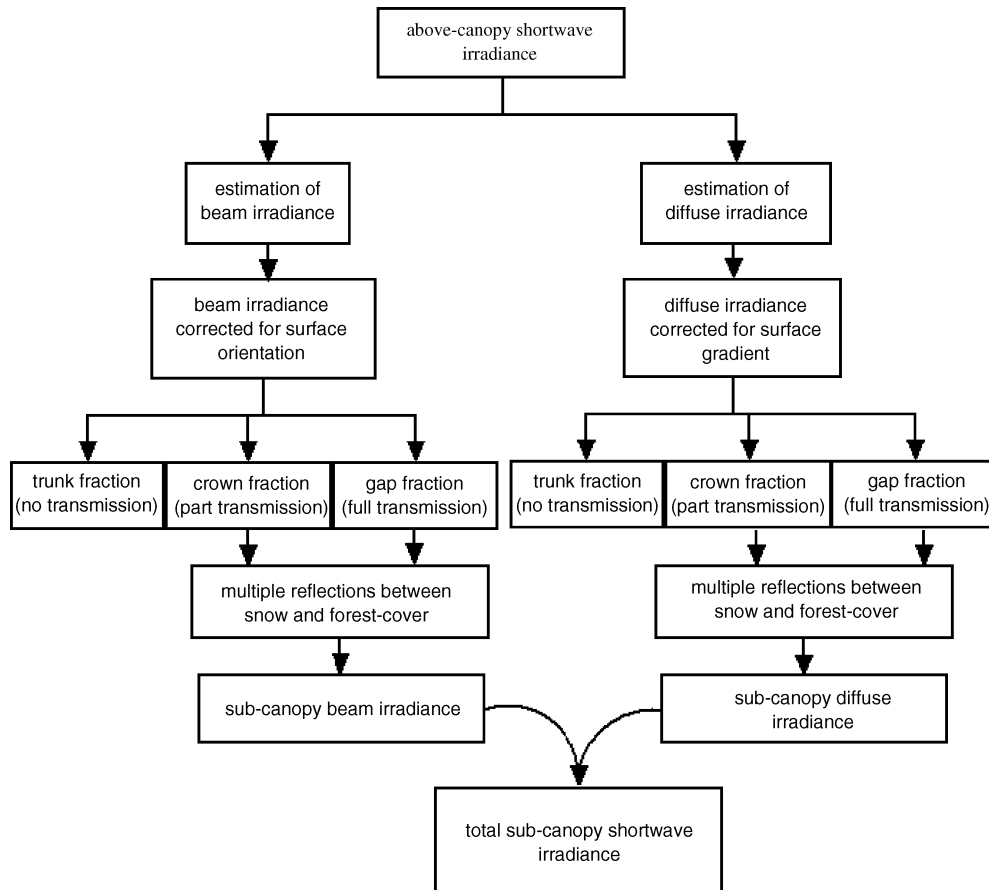
Figure 2. Schematic depicting main procedures and simulations products of the model
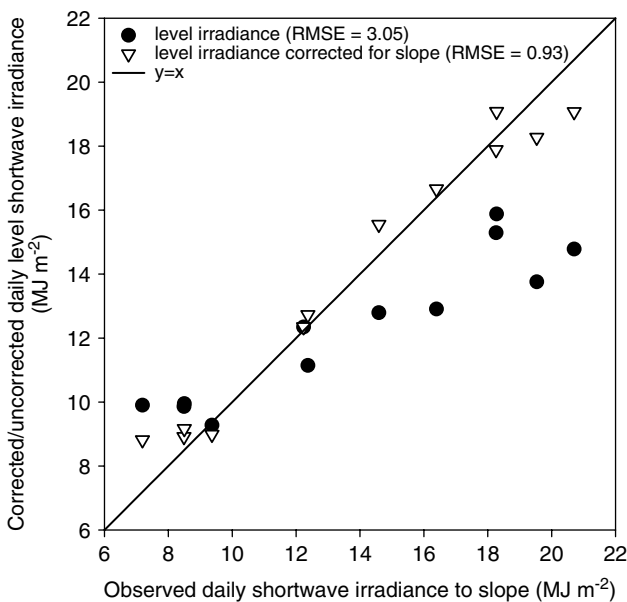

Figure 3. Scatterplot comparing observed daily shortwave irradiance to a slope of 27° slope gradient, 128° azimuth to corrected/uncorrected irradiance to a nearby level surface. RMSE is in MJ m^{-2} d^{-1}
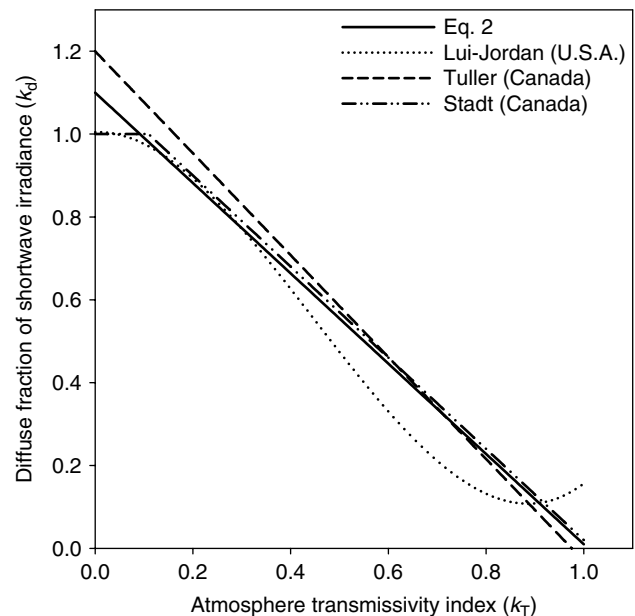

Figure 4. Correlations of diffuse shortwave irradiance fraction (k_d) to atmospheric transmissivity index (k_T) developed from measurements in Canada (Tuller, 1976; Stadt *et al*., 2005) and the United States (Lui and Jordan, 1960) compared to Equation (2)

and prolate spheroid crowns. The shadow cast from a single trunk/crown shape (x is used to denote either trunk or crown) consists of a component that may overlap with other shadows (x_O), and a non-overlapping component (x_{NO}) (Figure 5).

The fraction of horizontal surface area, H, occupied by multiple x_{NO} areas, (X_{NO}), cast from a ray received from sky elevation angle, θ, is equal to the sum of single
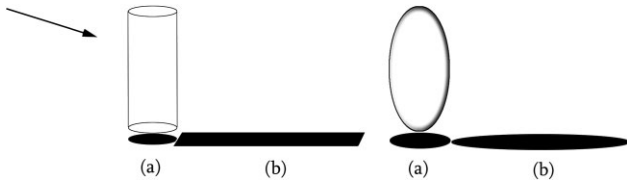
Figure 5. Illustration of the (a) non-overlapping (x_{NO}) and (b) overlapping (x_O) components of trunk (left) and crown (right) shadows projected upon a horizontal surface by their respective geometric shapes. Arrow indicates direction of incident shortwave ray

shadow areas as:

$$X_{NO}(\theta) = \frac{x_{NO}(\theta)n}{H} \tag{8}$$

where, n is the number of single non-overlapping shadow areas. By contrast, to determine the fraction of area H shaded by overlapping shadows, the amount of overlap must be accounted for. This is completed through the adaptation of the work of Satterlund (1983), in which the fraction of horizontal area H shaded by n overlapping shadows, (x_{NO}), is calculated by

$$X_O(\theta) = 1 - \exp\left(-\frac{x_O(\theta)n}{H}\right) \tag{9}$$

Thus, total X_f with respect to θ is given by the sum of the overlapping and non-overlapping shadow components,

$$X_f(\theta) = X_{NO}(\theta) + X_O(\theta) \tag{10}$$

$$= \frac{x_{NO}(\theta)n}{H} + 1 - \exp\left(-\frac{x_O(\theta)n}{H}\right) \tag{11}$$

The effect of surface orientation upon X_f is accounted for by multiplying H in Equation (11) by the slope correction factor, (scf), where:

$$scf = \frac{\cos(S^{\wedge}\Theta)}{\cos(H^{\wedge}\Theta)} \tag{12}$$

and $\cos(H^{\wedge}\Theta)$ is the cosine of the angle between the normal of horizontal surface, H, and irradiance received from position Θ of the sky hemisphere and $\cos(S^{\wedge}\Theta)$, the cosine of angle between the normal of surface of orientation S and Θ.

As $T_f = 0$, then $C_f = 0 \rightarrow 1$, and $G_f = 1$, transmissivity of irradiance through the entire forest-layer, τ, simplifies to

$$\tau = C_f \tau_{Cf} + G_f \tag{13}$$

in which τ_{Cf} is the transmissivity of the crown-fraction (calculation in next section). Assuming beam irradiance (K_B) is received only from the position of the solar disk (θ_S) and diffuse irradiance (K_B) is received in equal intensities from all sectors of the unobstructed sky hemisphere, then the respective forest transmissivities to beam (τ_B) and diffuse (τ_D) irradiance are described by Equations (14) and (15), respectively.

$$\tau_B = C_f(\theta_S)\tau_{Cf}(\theta_S) + G_f(\theta_S) \tag{14}$$

$$\tau_D = \int_0^{2\pi} d\hat{A} \int_0^{\pi/2} [C_f(\theta)\tau_{Cf}(\theta) + G_f(\theta)] \cos(\theta)\sin(\theta)\,d\theta \tag{15}.$$

Where $\hat{A}$ is the azimuth of the sky hemisphere from which irradiance is received. From this, forest transmissivity to total above-canopy shortwave irradiance is dependent upon the relative fraction of diffuse, k_d, and beam, $(1 - k_d)$, above-canopy components, where

$$\tau = [\tau_B(1 - k_d)][\tau_D(k_d)] \tag{16}.$$

Transmissivity of the forest crown-fraction

Transmissivity of shortwave irradiance through the crown forest-fraction (τ_{Cf}) is calculated using a Beer-Bouger-type formulation, expressed in its basic form as

$$\tau_{Cf} = \exp[-k\,\ell] \tag{17}$$

Here, the magnitude of shortwave irradiance entering C_f decreases exponentially with transmission path-length (ℓ) at a rate determined by the extinction coefficient k. Although useful, expressions such as Equation (17) do not fully account for physical processes of radiation transfer through crown foliage such as the multiple scattering of radiation between individual foliage element and the varying efficiencies to which differing spectra are transmitted through foliage.

Presuming a random spatial distribution of crown foliage, k in Equation (17) may be specified by the leaf-area-index parameter (LAI), equal to the total one-sided leaf area per unit ground area (Sicart *et al.*, 2004). However, in this case, because only transmittance through the crown-fraction is considered, LAI is scaled by the fraction of total horizontal forest area covered by crown foliage, C_C (i.e. LAI/C_C).

For needle-leaf trees, pronounced structuring of foliage necessitates further modification of k. Account for increased transmission through the C_f resulting from foliage aggregation (i.e. foliage self-shading) is made by the dimensionless foliage clumping parameter Ω, ranging from 0 (i.e. complete aggregation) to 1 (i.e. no aggregation). In addition, differential transmission of irradiance through the C_f with respect to θ resulting from the non-random vertical inclination of crown foliage is accounted for by the needle-leaf extinction efficiency parameter, $Q_{eff}(\theta)$:

$$Q_{eff}(\theta) = \cos(\beta^{\wedge}\theta) + b \tag{18}$$

where β is the normal angle to the average vertical inclination of foliage and $Q_{eff}(\theta)$ is equal to b when $\cos(\beta^{\wedge}\theta) = 0$. Here, it is assumed that $Q_{eff}(\theta)$ is invariable with respect to solar azimuth. This differs from the solar elevation dependent extinction efficiency formulation proposed by Pomeroy and Dion (1996) in that Pomeroy and Dion were attempting to account for differing beam paths through stems and jack pine foliage,

clumps and forest gaps with solar elevation, whereas this formulation is strictly for needle-leaf foliage.

For the case of a level ground surface, the transmission pathlength (ℓ) through C_f varies only with θ, and is determined by

$$\ell(\theta) = \ell_i(\theta)\ell_C(\theta) \qquad (19)$$

where $\ell_i(\theta)$ is the mean transmission pathlength through a single crown geometric shape traveled by irradiance received from θ, and $\ell_C(\theta)$ is the number of crown-overlaps apparent from θ corrected for the effect of slope by the *scf*, described by

$$\ell_C(\theta) = \rho(\theta)n \exp\left[-\frac{\rho(\theta)n}{H/scf}\right] \qquad (20)$$

in which $\rho(\theta)$ is the area of a single crown-shape apparent from sky elevation θ (calculation in appendix). With the above modifications to Equation (17) for foliage structuring and transmission pathlength, transmissivity of C_f to beam and diffuse irradiances are determined by Equations (21) and (22), respectively.

$$\tau_{Cf}(\text{beam}) = \exp\left[-\frac{LAI}{C_C}\Omega Q_{eff}(\theta_S)\ell(\theta_S)\right] \qquad (21)$$

$$\tau_{Cf}(\text{diffuse}) = \int_0^{2\pi} d\hat{A} \int_0^{\pi/2} \exp\left[-\frac{LAI}{C_C}\Omega Q_{eff}(\theta)\ell(\theta)\right] \\ \times \cos(\theta)\sin(\theta)\mathrm{d}\theta \qquad (22)$$

Backscattering of sub-canopy shortwave irradiance to snow

Estimation of the fraction of transmitted shortwave irradiance that is reflected back to the snow surface from the canopy (γ) is provided by the expression

$$\gamma = \sum_{i=1}^{n}(\alpha_S C c \alpha_C)^i \qquad (23)$$

where α_C is the bulk-canopy foliage albedo, set at 0·15 according to many observations over a jack pine forest by Pomeroy and Dion (1996), α_S is the snow surface albedo which may be set by *in situ* measurements or modelled (e.g. Hardy *et al.*, 1998; Melloh *et al.*, 2002). Although radiation may be reflected between the snow and canopy numerous times, shortwave irradiance enhancement to snow beyond third-order scattering (i.e. $n > 3$) is minor and is ignored in Equation (23) as sensitivity analysis demonstrated this provided negligible additional irradiance to snow ($<0·1$ W m^{-2}) for reasonable set values of α_C, α_S and C_C. However, it should be noted that Eq. 23 may also be solved explicitly following that of Nijssen and Lettenmaier (1999). The underlying assumptions of Equation (23) are that diffuse and beam irradiances are scattered by sub-canopy snowcover and foliage with equal efficiency, and that backscattering occurs only from the horizontal crown component (i.e. C_C) of the forest-layer.
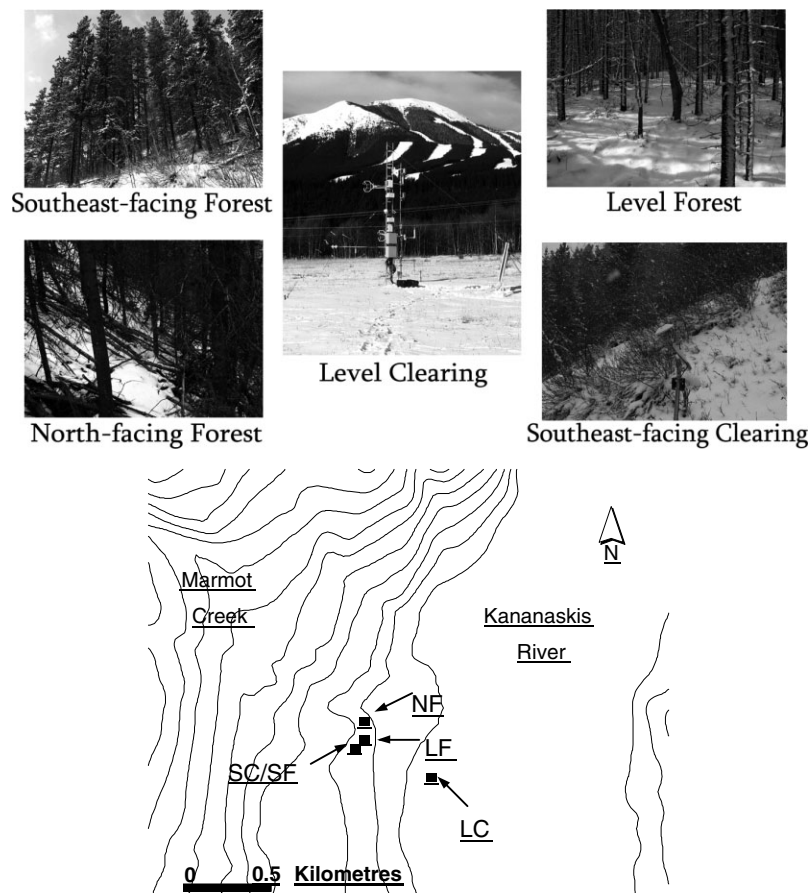

Figure 6. Photographs (top) and locations (bottom) of observation sites within the Marmot Creek Research Basin, Alberta, Canada. Contour intervals are 50 m

MODEL APPLICATION

Estimates of daily sub-canopy shortwave irradiance were made at three forest sites with a melting snowcover within the Marmot Creek Research Basin (50° 57′N, 115° 09′W) located in the Rocky Mountains of southern Alberta, Canada. Sub-canopy shortwave irradiance was measured by recently calibrated Kipp and Zonen pyranometers inclined parallel to the respective ground surfaces at:

(1) a southeast facing forest (26° slope, 125° azimuth) with discontinuous canopy cover and non-uniform tree size; 1563 m.a.s.l.; average daily surface albedo of 0·55; hereafter referred to as the SF,
(2) a north facing forest (29° slope, 351° azimuth) with continuous canopy-cover and uniform tree size; 1490 m.a.s.l; mean daily surface albedo of 0·60; hereafter referred to as the NF, and
(3) a level forest with continuous canopy-cover and uniform tree size; 1528 m.a.s.l.; mean daily surface albedo of 0·7; hereafter referred to as the LF.

Shortwave irradiance was also observed at the following clearing sites:

(4) a level clearing; sky view factor of 0·98; 1457 m.a.s.l.; mean daily surface albedo of 0·75; hereafter referred to as the LC, and
(5) a clearing of southeast sloping orientation (27° slope, 128° azimuth); adjacent to SF; sky-view factor of 0·8; 1566 m.a.s.l.; hereafter referred to as the SC.

Sub-canopy irradiance was measured at each site by a single pyranometer, with the exception of the SF where two additional sensors were deployed because of the discontinuous forest-cover. Photographs and locations of the above sites within the Marmot Creek Research Basin are shown in Figure 6.

Errors in shortwave irradiance observations

As pointed out by Moore and Rowland (1990), observed data may be subject to instrument and/or sampling error, both of which may contain systematic and random components. For this study however, systematic instrument errors are ignored as all sensors had been recently calibrated and therefore assumed unbiased. As a result, instrument error is considered solely random in nature with tolerance levels assigned as those specified by the manufacturer in ± percentage of daily irradiance.

Sub-canopy irradiance was measured by only a single sensor at the NF and LF sites and by three sensors at the SF; as a result, considerable sampling error may also affect the reliability of observations. To assess the extent of sampling error of the single sensors (hereafter referred to as 'site' sensors), daily irradiance was compared to measurements by a 10-sensor array, of which all sensors had been recently calibrated and positioned randomly at the SF and LF sites (array not deployed at the NF due to the hazardousness of the site). Accordingly, the array is assumed to exhibit no systematic instrument or sampling biases. Random sampling errors by the array were also ignored due to the long sampling interval (i.e. daily) of the observations, which relative to short time intervals (e.g. 15 min, 1 h) greatly reduces the spatial variability of sub-canopy irradiance caused by small-scale heterogeneity in forest-cover density (Rowlands *et al.*, 2002). Errors in array observations are therefore expected to exist only as random instrument errors. Table I shows the instrument errors expected for all sensors used, as well as the relative expected sampling error (RESE) for the SF and LF sites, determined by:

$$\text{RESE} = \frac{\text{RMSE(array} - \text{single sensor daily irradiance)}}{\text{array daily irradiance}}$$

(24)

From the determined instrument and sampling errors, the mean and maximum expected observation errors are provided in Table I, expressed both as a fraction of daily irradiance and absolute irradiance.

Model parameterization

Estimates of the biophysical parameters LAI, clumping index, Ω, crown-cover fraction, C_C, and average leaf inclination angle, ALA, were provided by hemispherical

Table I. Expected instrument and sampling errors of shortwave irradiance at southeast-facing forest (SF), level forest (LF), and southeast-facing clearing (SC) sites. All errors are expressed as a fraction of daily irradiance (K_{day}) with the exception of the mean expected observation error which is also expressed in terms of absolute irradiance (MJ m^{-2} d^{-1}), which at the forest sites is equal to array daily irradiance. Maximum expected observation error is equal to the sum of the array sensor error, the expected site sensor error, and the expected sampling error. At the SF site mean daily irradiance of the three site sensors was used as this provided the best comparison to array irradiance

Site	Sensor class[a]	Expected array Sensor error[b]	Expected site Sensor error[b]	Relative expected Sampling error	Maximum expected Observation error	Mean expected Observation error	Mean daily Irradiance (MJ m^{-2} d^{-1})	Mean expected Error (MJ m^{-2} d^{-1})
LC	2	—	±0·10 K_{day}	—	±0·10 K_{day}	±0·10 K_{day}	12·3	±0·12
SF	2	±0·05 K_{day}	±0·05 K_{day}	±0·05 K_{day}	±0·15 K_{day}	±0·08 K_{day}	4·22	±0·34
LF	2	±0·10 K_{day}	±0·10 K_{day}	±0·19 K_{day}	±0·39 K_{day}	±0·13 K_{day}	1·92	±0·19
SC	1	—	±0·02 K_{day}	—	±0·02 K_{day}	±0·02 K_{day}	14·0	±0·28

[a] According to WMO standard.
[b] As stated by the manufacturer.

photograph analysis using CAN-EYE software (Baret and Weiss, 2004; Weiss *et al.*, 2004; Jonckheere *et al.*, 2004). By determining the forest gap-fraction of each pixel within the forest image, CAN-EYE calculates LAI and ALA through the inversion of the Poisson model in which foliage inclination is assumed to follow an ellipsoid distribution. The foliage clumping index is determined using the Lang and Yueqin (1986) logarithm gap fraction averaging method.

This particular software was used for its ability to discriminate between trunk and crown foliage material, allowing separate analysis of each. CAN-EYE also permits the analysis of up to 16 images simultaneously, providing an assessment of each forest stand as a whole. Biophysical estimates of crown foliage at the SF, LF and NF sites by hemispherical image analysis are given in Table II.

Parameterization of the dimensions of the trunk and crown geometric shapes was performed using forest-survey data. Individual trees greater than 2 m height at each forest site were surveyed for total height, crown height, maximum crown width, average tree-spacing, and diameter at breast height (dbh) within an area of 400 m^2 surrounding each radiation sensor. Trunks were abstracted as right-circular cylinders and crowns as prolate spheroids. The dimensions of the trunk and crown shapes at each forest site were specified by: (i) the arithmetic mean (ii) the maximum value and (iii) the mean weighted by rank of the datum value (greatest weight to largest dimensions) within the sample.

Simulations of daily K_S were performed for all forest sites using the trunk and crown geometric shape dimensions specified by (i), (ii) and (iii) above at a resolution of 5° for both sky elevation and azimuth angles. Comparisons of observed K_S to simulated K_S using all three forest-survey data processing methods were made by the model efficiency index (MEI):

$$\text{MEI} = 1 - \left[\frac{\sum\limits_{i=1}^{n}(x_{\text{obs}} - x_{\text{mod}})^2}{\sum\limits_{i=1}^{n}(x_{\text{obs}} - x_{\text{avg}})^2} \right] \quad (25)$$

With the exception of the NF, best simulations of K_S were made using the weighted mean of forest-survey data
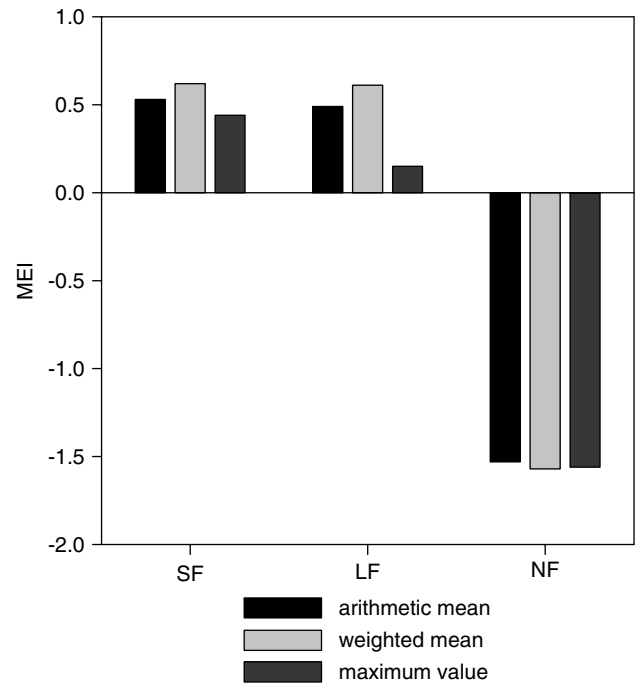

Figure 7. Model efficiency index (MEI) of observed daily shortwave transmittance for forests of southeast-facing (SF), level (LF), and north (NF) orientations to simulations using trunk and crown shape dimensions specified by the (i) arithmetic mean (ii) maximum value and (iii) weighted mean of forest-survey data

for all sites (Figure 7). Simulations using the weighted-mean of forest survey data are shown compared to observed daily K_S for all forests sites in Figure 8.

Simulations of daily K_S using the weighted-means of forest-survey data were compared to observations of daily K_S by the RMSE. Greatest RMSE occurred for simulations at the SF, equalling 0·64 MJ m^{-2}d^{-1}, compared to 0·44 MJ m^{-2}d^{-1} at the level forest, and 0·27 MJ m^{-2}d^{-1} at the north-facing forest.

Further evaluation of the model is provided by comparing simulated and observed forest transmissivities (τ) with respect to elevation angle (from the horizon) and azimuth of the sky hemisphere. Figure 9 shows simulations of τ throughout the sky hemispheres of all forest sites as compared to values provided by CAN-EYE hemispherical photograph analysis. For all sites, simulated transmissivity values with sky position are shown to roughly correspond to the outputs from photograph

Table II. Crown foliage bio-physical parameters estimated from hemispherical photographs by CAN-EYE analysis software for southeast-facing forest (SF), level forest (LF) and north-facing forest (NF) sites

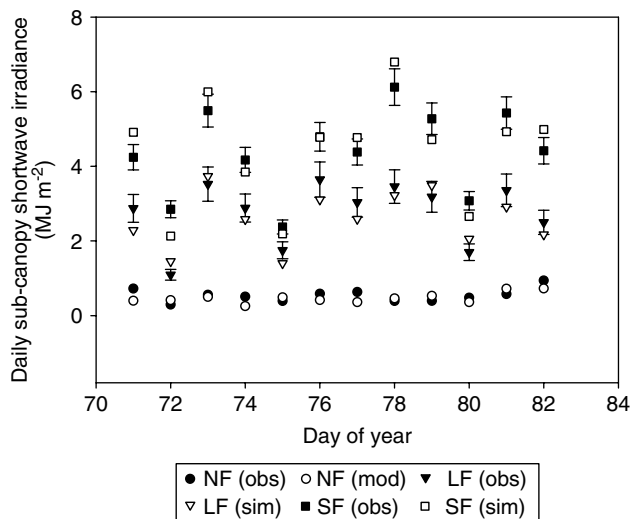| Biophysical parameter	Site		
	SF	LF	NF
Number of hemispherical photographs analyzed	14	12	12
fraction of crown coverage (C_C)	0·66	0·69	0·79
crown LAI (m^2/m^2)	0·71	0·82	0·9
average leaf inclination angle from zenith (°°)	60	72	60
foliage clumping index (Ω)	0·86	0·97	0·95

Figure 8. Observed (obs) and modelled (mod) daily shortwave sub-canopy irradiance for southeast-facing (SF), level (LF) and north-facing (NF) forest sites (vertical bars denote the mean expected observation error as shown in Table I)

analysis. At the LF site, simulated and photograph analysis outputs show little preference in τ values with respect to sky azimuth, but does progressively increase with sky elevation in both. By contrast, at the sloping sites, simulated and photograph outputs show increased τ values occurring at sky azimuths corresponding to their respective slope azimuths. By including the position of the solar disk within the sky hemisphere in Figure 10, both the observed and simulated images suggest that greatest transmittance of beam irradiance is to occur at the SF and least amount of beam transmittance to occur at the NF.

Sensitivity analysis

To illustrate the effect of forest-cover density on daily τ with respect to surface orientation, model simulations were performed for forests of north, east, south and west orientations at slope gradients of $10°$, $25°$ and $40°$. Here, changes in forest-cover density are made through modification of forest-stocking density where a density of one is equal to the mean value of the three forest sites: a single tree per 6.2 m^2 of the following
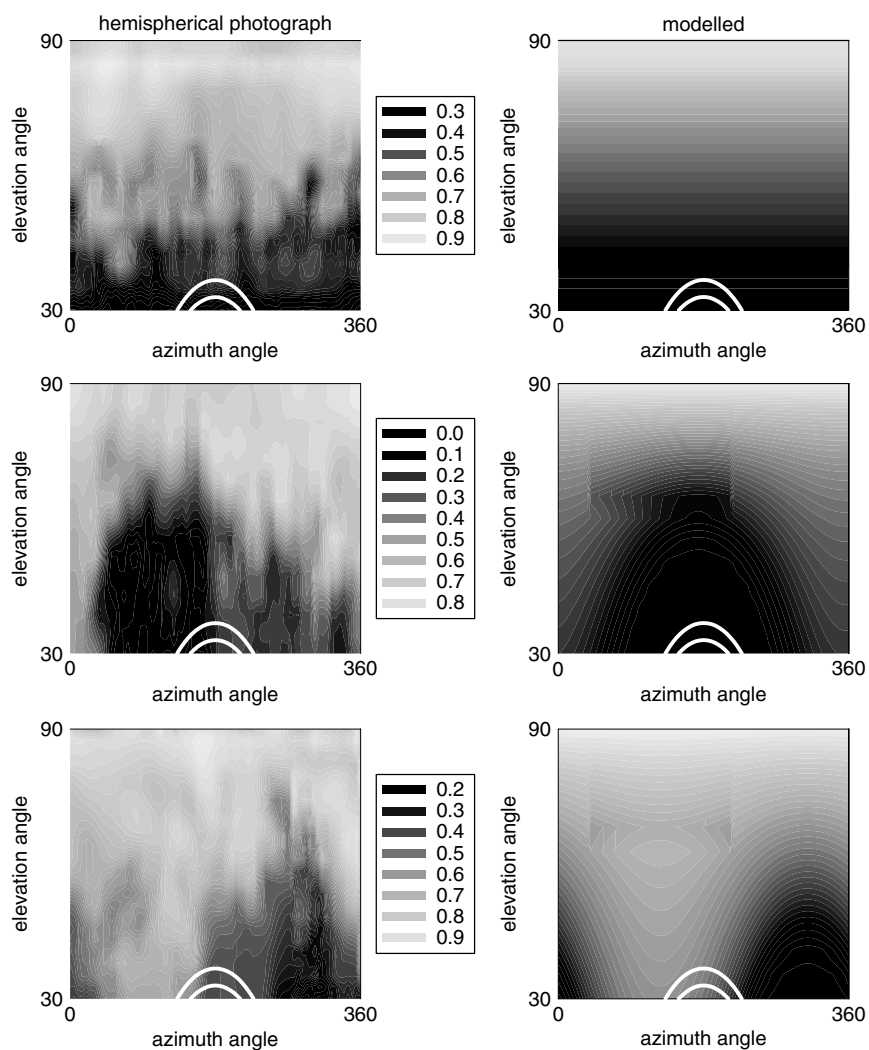

Figure 9. Forest shortwave irradiance transmissivity with respect to elevation and azimuth of sky hemisphere as determined from hemispherical photograph analysis by CAN-EYE software (left) and model simulations (right) for LF (top), NF (middle) and SF (bottom) sites (range of daily migration of solar disk during the observation period is delimited by solid white line)
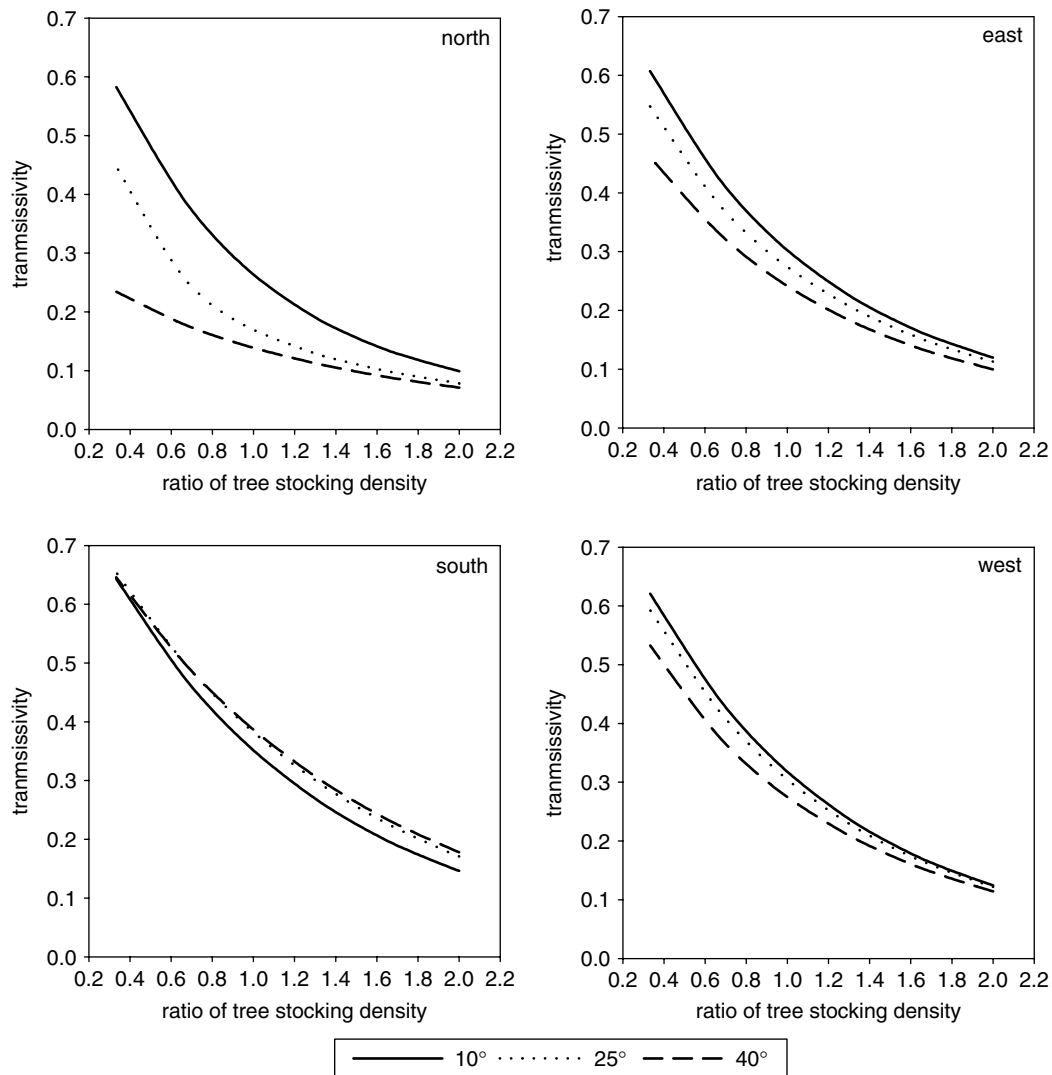
Figure 10. Sensitivity of shortwave transmissivity through forest-cover with change in tree-stocking density for forests on slope-gradients of 10°, 25° and 40° facing: north, east, west and south directions

dimensions: trunk height $= 10$ m, trunk width $= 10$ cm, crown height $= 3$ m, crown width $= 0.5$ m. All other forest parameters (i.e. LAI, Ω, ALA) were held constant and set identical for all sites. Simulations were made using above-canopy irradiance from DOY 81, which was closest to the mean daily irradiance of the entire observation period. Figure 10 shows that, overall, the south-facing, west- and east-facing forests exhibited the greatest sensitivity in τ to change in forest-stocking density, but exhibited little sensitivity to change in slope-gradient. At the north-facing forest, τ simulations showed little sensitivity to forest-stocking densities at high coverage, but at low coverage, there is a marked increased in τ with decreasing stocking-densities for all slope gradients.

DISCUSSION

Amongst forest sites, differences in both forest-cover density and surface orientation produced substantial variation in the amounts of shortwave irradiance to the sub-canopy surface. Attenuation of irradiance by forest-cover further accentuates differences in irradiance energy from that which would be expected from orientation effects alone. At the SF, decreased forest-cover, shorter transmission pathlength through crown foliage and larger gap fraction along the beam-path resulted in the highest transmittance of irradiance amongst the forest sites. Due to increased transmission of beam irradiance, transmissivity values and sub-canopy irradiance at the SF also exhibited the greatest variation with change in the relative amounts of above-canopy diffuse and beam irradiance resulting from differing sky conditions (e.g. cloud-cover). By contrast, due to the small amount of beam transmittance at the NF, little variation in sub-canopy irradiance was observed at this site.

From model results, transmission of above-canopy shortwave irradiance through south-facing forests is expected to display considerable sensitivity to change in forest-cover density and due to increased above-canopy irradiance, even greater sensitivity in terms

of absolute sub-canopy irradiance. Alternatively, sub-canopy irradiance at north-facing forests is likely to show less sensitivity to change in forest-cover density due to decreased variation in transmissivity and reduced incident above-canopy irradiance. According to model sensitivity analysis, small changes in cover-density in continuous north-facing forests are likely to cause little change in sub-canopy irradiance. It is suggested that only for much sparser canopy coverage, can changes in forest-cover density for north-facing forests produce substantial changes in sub-canopy irradiance. Since shortwave irradiance is a major component of melt energy, these findings imply that the degree of change in the timing and rate of mountain snowmelt brought on by forest-cover reductions (e.g. clear-cutting, forest disease and infestation) may depend strongly on the slope and aspect of the forest stand.

As the final simulation product of the model is that of sub-canopy shortwave irradiance, no explicit account is given for highly-complex processes such as multiple scattering of irradiance within and between tree crowns (e.g. Ni *et al*., 1999). Instead, transmission of above-canopy irradiance through crown foliage is determined through use of a modified Beer-Bouger expression, accompanied by a number of simplifying assumptions that limits its representation of the physical radiative-transfer processes by the model. However, this also serves to reduce the complexity of the model, allowing easier application.

In terms of potential radiation energy available for snowmelt, model simulations errors were greatest at the southeast-facing forest, equal to approximately 3 MJ m^{-2} over the twelve day period. Also, for most days at the southeast-facing and level forest sites, simulations errors exceeded that of the expected observation error. However, considering sub-canopy snow in mountain regions typically reach seasonal accumulations of 25 to 55 mm SWE (Jeffery, 1965) and most irradiance is reflected from snow, errors in net sub-canopy shortwave energy for melt are likely to be much more modest. Thus, in combination with reliable simulation of snow albedo and longwave radiation energy this model may be a useful in predicting sub-canopy snowmelt in mountain forests, and identifying potential change in snowmelt timing and magnitude with differing forest-cover densities.

A major drawback of the model is that of the high number of parameters requiring specification from forest and terrain inventories and hemispherical photograph analysis. Although parameters such as stocking density and tree height/widths are commonly included in standard forest inventories, leaf-area-index and the foliage aggregation index estimates are not, and are difficult to obtain at landscape or regional scales. Alternatively, use of developing remote-sensing technologies such as scanning LiDAR have shown increased potential, especially in low-density forests such as lodgepole-pine, in providing information such as trunk and crown

dimensions (Lefsky *et al*., 1999). Biome-specific forest allometric relationship may prove useful in estimating many of the parameters from simple measures such as stocking density in regional applications. It is likely that further application of the model over larger spatial-scales would benefit from the incorporation of wide-scale forest information such as that provided by LiDAR.

CONCLUSIONS

From comparisons to observations, the model outlined in this paper provides reasonable simulations of sub-canopy shortwave irradiance for forests of differing slope, aspect and cover-density for the purpose of estimating sub-canopy snowmelt. Model simulations adequately represented the differences in daily shortwave transmissivity and sub-canopy irradiance amongst forest sites. However, the model abstracts the forest-layer as equally-spaced trees of identical dimensions, and therefore cannot fully represent the heterogeneity of forest-cover for irradiance received by all sectors of the apparent sky hemisphere. No significant change in model performance was detected amongst all forest sites with change in cloud cover and the relative fractions of diffuse and beam irradiance. Although the greatest simulation errors relative to mean irradiance occurred for the north-facing forest, errors in terms of absolute irradiance were small at this site due to decreased above-canopy irradiance. In contrast, for the southeast-facing forest, where sub-canopy irradiance was much greater, the model gave improved relative estimates despite the discontinuous forest-cover, but gave larger errors in terms of absolute sub-canopy irradiance.

The best simulations from the model were provided by forest-shapes described by a dimension ranging from the arithmetic mean to the maximum value of forest mensuration data. It is hypothesized that this is due to larger trunks and crowns having greater effect upon irradiance extinction than those of smaller dimensions, while at the same time, maximum forest mensuration values over-estimating the amount of forest extinction. However, further investigation is required to determine whether similar results are found for simulations of other forest sites and whether the use of a single, simple forest-survey data pre-processing method can be recommended in general. The model has a large number of forest mensuration parameters; hence application over larger spatial-scales would benefit from developing remote-sensing technologies such as LiDAR and from use of biome specific forest mensuration relationships.

Modelled and observed results indicate that sub-canopy shortwave irradiance snowmelt energy is likely to exhibit the greatest variation with change in sky condition and forest-cover density under south-facing forests and

the least variation under north-facing forests. This suggests the timing of snowmelt may exhibit greater variation for forests of more south-facing orientations compared to more north-facing orientations, which is important for the up-scaling of point snowmelt simulations for prediction of snowmelt across forested mountain basins.

NOTATION

$\hat{A}$	sky hemisphere azimuth [radians]
b	foliage extinction efficiency at $\cos(\beta^{\wedge}\theta) = 0$ [dimensionless]
α_S	snow surface albedo [dimensionless]
α_C	forest foliage albedo [dimensionless]
$\hat{\beta}$	normal angle to average vertical foliage inclination [radians]
C_f	forest crown-fraction [dimensionless]
C_C	horizontal canopy-cover [dimensionless]
Δ	slope gradient from horizontal [radians/degrees]
δ	solar declination [radians]
G_f	forest gap-fraction [dimensionless]
γ	fraction of transmitted shortwave irradiance backscattered to snow surface [dimensionless]
$Q_{eff}(\theta)$	needle-leaf foliage extinction efficiency parameter [dimensionless]
H	horizontal unit-area [dimensionless]
I_O	solar constant [4·921 MJ m^{-2} h^{-1}]
K_B	above-canopy beam irradiance [Flux L^{-2}]
k_b	fraction of beam to total shortwave irradiance [dimensionless]
K_D	above-canopy diffuse irradiance [Flux L^{-2}]
k_d	diffuse fraction of shortwave irradiance [dimensionless]
K_{EX}	exo-atmospheric shortwave irradiance [Flux L^{-2}]
$K_{O(Level)}$	above-canopy shortwave irradiance received at a level surface [Flux L^{-2}]
$K_{O(Slope)}$	above-canopy shortwave irradiance received at a surface of orientation S [Flux L^{-2}]
K_S	sub-canopy shortwave irradiance [Flux L^{-2}]
k_T	atmospheric transmissivity (clearness) index [dimensionless]
LAI	leaf-area-index [dimensionless]
LC	level clearing site
LF	level forest site
$\ell_C(\theta)$	mean crown overlap apparent from sky elevation angle θ [dimensionless]
$\ell_i(\theta)$	mean transmission pathlength through a single crown [L]
MBE	mean bias error
MEI	model efficiency index
n	quantity [dimensionless]
NF	forest site of north sloping orientation
Ω	foliage aggregation index [dimensionless]
ϕ	hour angle from solar noon [radians]
Φ	latitude [radians]
π	pi
scf	geometric slope correction factor [dimensionless]
SC	clearing site of southeast orientation
SF	forest site of southeast sloping orientation
T_f	forest trunk-fraction [dimensionless]
τ_B	forest transmissivity of beam shortwave irradiance [dimensionless]
τ_D	forest transmissivity of diffuse shortwave irradiance [dimensionless]
τ_{Cf}	shortwave irradiance transmissivity of forest crown-fraction [dimensionless]
τ	forest transmissivity to above-canopy shortwave irradiance [dimensionless]
θ	elevation angle above horizon [radians]
θ_S	elevation angle of solar disk above horizon [radians]
Θ	sky position $(\theta, \hat{A})$ [radians]
x_O	ground surface area shaded by a single overlapping shadow component [L^{-2}]
x_{NO}	ground surface area shaded by a single non-overlapping shadow component [L^{-2}]
X_O	fraction of ground surface area shaded by overlapping shadows [dimensionless]
X_{NO}	fraction of ground surface area shaded by non-overlapping shadows [dimensionless]
x_{mod}	modelled variable value
x_{obs}	observed variable value
RESE	relative expected sampling error [fraction of daily shortwave irradiance]
RMSE	root mean square error
Z	angle from zenith of sky hemisphere [radians]
$^{\wedge}$	operator denoting angle between 2 vectors [dimensionless]

REFERENCES

Baret F, Weiss M. 2004. *CANEYE Hemispherical Photograph Analysis Software*. Avignon, l' Institut National de la Recherch Agrinomique (INRA). <can-eye@avignon.inra.fr.>, First accessed: 02/02/2006.

Corbaud B, Coligny F, Cordonnier T. 2003. Simulating radiation distribution in a heterogeneous Norway spruce forest on a slope. *Agricultural and Forest Meteorology* **116**: 1–18.

Federer CA. 1968. Radiation and snowmelt on a clearcut watershed. In *Proceedings of the 25th eastern snow conference*, Boston, MA, 28–42.

Federer CA. 1971. Solar radiation absorption by a leafless hardwood forest. *Agricultural Meteorology* **9**: 3–20.

Hardy JP, Davis RE, Jordan R, Ni W, Woodcock C. 1998. Snow ablation modelling at the stand scale in a boreal jack pine forest. *Hydrological Processes* **12**(10/11): 1763–1778.

Jeffery WW. 1965. Snow hydrology in the forest environment. *Proceedings of the Workshop Seminar: Snow Hydrology*. Canadian National Committee for the International Hydrological Decade, University of New Brunswick: Canada; 1–19.

Jonckheere I, Fleck S, Nackaerts K, Muys B, Coppin P, Weiss M, Baret F. 2004. Methods for leaf area index determination. Part I: Theories, techniques and instruments. *Agricultural and Forest Meteorology* **121**: 19–35.

Lang ARG, Yueqin X. 1986. Estimation of leaf area index from transmission of direct sunlight in discontinuous canopies. *Agricultural and Forest Meteorology* **37**: 229–243.

Lefsky MA, Cohen WB, Acker SA, Parker GG, Speies TA, Harding D. 1999. Lidar remote sensing of the canopy and biophysical properties of Douglas Fir-Western Hemlock forests. *Remote Sensing of Environment* **70**: 339–361.

Link T, Marks D. 1999. Point simulation of seasonal snow cover dynamics beneath boreal forest canopies. *Journal of Geophysical Research* **104**: 27841–27857.

Lui BYH, Jordan RC. 1960. The interrelationship and characteristic distribution of direct, diffuse and total solar radiation. *Solar Energy* **4**(1): 1–19.

Marks D, Winstral A. 2001. Comparison of snow depositions, the snowcover energy balance, and snowmelt at two sites in a semi-arid mountain basin. *Journal of Hydrometeorology* **2**: 213–227.

Melloh R, Hardy J, Bailey R, Hall J. 2002. An efficient snow albedo model for the open and sub-canopy. *Hydrological Processes* **16**: 3571–3584.

Melloh R, Ballard J, Hardy J, Woodcock C, Liu J, Smith J, Koenig G, and R Davis. 2003. Spatial distribution of canopy gaps in lodgepole pine forest. In *Proceedings of the 60th eastern snow conference*, Sherbrooke, Quebec, Canada, 111–123.

Moore RD, Rowland JD. 1990. Evaluation of model performance when observed data are subject to error. *Physical Geography* **11**(4): 379–392.

Ni W, Li X, Woodcock CE, Caetano MR, Strahler AH. 1999. An analytical hybrid GORT model for bidirectional reflectance over discontinuous plant canopies. *IEEE Transactions on Geoscience and Remote Sensing* **37**(2): 987–999.

Nijssen and Lettenmaier DP. 1999. A Simplified Approach for Predicting Shortwave Radiation Transfer Through a Forest Canopy. *Journal of Geophysical Research* **104**(D22): 27859–27868.

Pomeroy JW, Dion K. 1996. Winter irradiance extinction and reflection in a boreal pine canopy: measurements and modelling. *Hydrological Processes* **10**: 1591–1608.

Rowland JD, Moore RD. 1992. Modelling solar irradiance on sloping surfaces under leafless deciduous forests. *Agricultural and Forest Meteorology* **60**: 111–132.

Rowlands A, Pomeroy J, Hardy J, Marks D, Elder K Melloh R. 2002. Small-scale spatial variability of radiant energy for snowmelt in a mid-latitude sub-alpine forest. In *Proceedings of the eastern snow conference* **59**: 109–117.

Satterlund DR. 1983. Forest shadows: How much shelter in a shelterwood? *Forest Ecology and Management* **5**: 23–37.

Sicart JE, Pomeroy JW, Essery RLH, Hardy JE, Link T, Marks D. 2004. A sensitivity study of daytime net radiation during snowmelt to forest canopy and atmospheric conditions. *Journal of Hydrometeorology* **5**: 774–784.

Stadt KJ, Lieffers VJ. 2000. MIXLIGHT: a flexible light transmission model for mixed species forest stands. *Agricultural and Forest Meteorology* **102**: 235–252.

Stadt KJ, Lieffers VJ, Hall RJ, Messier C. 2005. Spatially explicit modeling of PAR transmission and growth of *Picea glauca* and *Abies balsamea* in the boreal forest of Alberta and Quebec. *Canadian Journal of Forest Research* **35**: 1–12.

Tuller SE. 1976. The relationship between diffuse, total and extraterrestrial solar radiation. *Solar Energy* **18**: 259.

United States Army Corps of Engineers. 1956. *Snow Hydrology: Summary Report of the Snow Investigations*. Portland, Oregon, North Pacific Division, US Army Corps of Engineers 437.

Wang Q, Tenhunen J, Schmidt M, Kolcun O, Droesler M. 2006. A model to estimate shortwave irradiance in complex terrain. *Boundary-Layer Meteorology* **119**: 409–429.

Weiss M, Baret F, Smith GJ, Jonckheere I. 2004. Methods for in situ leaf area index measurement, part II: from gap fraction to leaf area index: retrieval methods and sampling strategies. *Agricultural and Forest Meteorology* **121**: 17–53.

Williams LD, Barry RG, Andrews JT. 1972. Application of computed shortwave radiation for areas of high relief. *Journal of Applied Meteorology* **11**: 526–533.

APPENDIX: CALCULATIONS

Geometric correction of above-canopy short-wave irradiance from a level surface $K_{O(Level)}$ to a sloped surface $K_{O(Slope)}$ is provided by

$$K_{o(Slope)} = k_b K_{o(Level)} scf + k_d K_{o(Level)} \left(1 - \frac{\Delta}{\pi} \right) \tag{A1}$$

where the slope correction factor (scf) is determined

$$scf = \frac{\cos(S^\wedge \Theta)}{\cos(H^\wedge \Theta)} \tag{A2}$$

in which the cosine between the vector of beam irradiance received from sky position Θ and surface of a given slope gradient and azimuth (denoted here as Z) is calculated by Williams *et al.* (1972) expression:

$$\cos(Z^\wedge \Theta) = [c_1 \sin \varphi + c_2 \cos \varphi + c_3] d\varphi \tag{A3}$$

where

$$c_1 = -\sin(A)\sin(\Delta)\cos(\delta)$$

$$c_2 = [(\cos(\Phi)\cos(\Delta) - \sin(\Phi)\cos(A)\sin(\theta)]\cos(\delta)$$

$$c_3 = [(\sin(\Phi)\cos(\Delta) + \cos(\Phi)\cos(A)\sin(\theta)]\sin(\delta)$$

and

$\hat{A}$ = azimuth angle of sky hemisphere from which irradiance is received

ϕ = hour angle measured from solar noon

δ = solar declination

Φ = latitude

Δ = slope gradient of surface from horizon

Z = zenith angle of sky hemisphere from which irradiance is received

Calculation of exo-atmospheric shortwave irradiance (K_{EX}) from time t to t' is performed by

$$K_{EX} = \frac{I_O}{r^2} \int_t^{t'} \cos(H^\wedge \Theta) dt \tag{A4}$$

where I_O is the solar constant, equal to 4·921 MJ m^{-2} h^{-1} and r is the Earth-sun radius vector.

Calculation of crown path-length and overlap:

The average single crown path-length $\ell_i(\theta)$ is determined as the ratio of crown shape volume (V_C) to area of the crown apparent from θ, $\rho(\theta)$. In the case where crowns are abstracted by a prolate spheroid $\ell_i(\theta)$ is determined as the ratio of a single spheroid volume to that of the area of single spheroid apparent from θ:

$$\ell_i(\theta) = \frac{V_C}{\rho(\theta)} = \frac{2\pi a^2 b}{3\rho(\theta)} \quad \text{(A5)}$$

where a and b are the respective minor (horizontal) and (major vertical) axes of the prolate spheroid and $\rho(\theta)$ is given by:

$$\rho(\theta) = \{a\sin(\theta) + [a^2 \sin 2(\theta) + b^2 \cos^2(\theta)]^{1/2}\}\pi a/2 \quad \text{(A6)}$$